An Assessment of the Impact of Satellite Microwave Sounder Incidence Angle and Scan Geometry on the Accuracy of Atmospheric Temperature Profile Retrievals

P. W. ROSENKRANZ

Research Laboratory of Electronics, Massachusetts Institute of Technology, Cambridge, Massachusetts

K. D. HUTCHISON, K. R. HARDY, AND M. S. DAVIS

Center for Remote Environmental Sensing Technology, Lockheed Martin Missiles and Space, Sunnyvale, California

(Manuscript received 15 May 1996, in final form 25 October 1996)

ABSTRACT

Cross-track and conical scan microwave sounder designs are compared with respect to temperature profile retrieval accuracy in nonprecipitating atmospheres and with respect to the beamfilling effect of precipitation. The conical design shows slightly better accuracy at pressure levels of 3 hPa or less, while the cross-track design performs slightly better at pressure levels of 850 hPa or greater. Under the assumption that precipitation-contaminated fields of view would be rejected, consideration of beamfilling by rain cells indicates that retrieval yield would be higher for the cross-track design.

1. Introduction

Three distinct scan designs have been developed for satellite-based microwave sensors: cross-track, in which the angle of earth incidence varies and passes through nadir; conical, which has a fixed angle of incidence and a vertical axis of rotation; and limb-scanning, which has a narrow range of near-tangent incidence angles. Given adequate antenna size to take advantage of their respective geometries, the two downward-pointing modes typically offer better horizontal spatial resolution, whereas limb scanning offers better vertical resolution. An instrument designer's choice between limb scanning and one of the other modes would largely be made on the basis of that trade-off, but a decision between cross-track and conical scan involves several issues. The purpose of this paper is to compare the latter two scan modes with respect to temperature-profile retrieval accuracy, by means of simulations. We will not further discuss limb-scanning here, but a description of the technique can be found in Waters (1993).

Bearing on the choice between cross-track and conical scan are the following points.

(a) With increasing incidence angle θ (measured from vertical at the surface), the peak altitude of a temperature weighting function increases, and to some extent its vertical width changes. (These changes are described in more detail in section 2.) To obtain contiguous swath coverage at the equator, from the usual weather satellite polar orbit altitude of 833 km, requires max(θ) ∼ 70°. [The currently operational Special Sensor Microwave/Imager (SSM/I) utilizes a 53° incidence angle and hence does not provide contiguous coverage.] Because the cross-track instrument should provide good retrievals over its entire range of incidence angles, its frequencies are chosen to obtain weighting functions that penetrate to the bottom of the atmosphere at the maximum incidence angle. Hence, both scan designs considered here use the same channels for sounding the lower atmosphere. There is one difference in the channel set at the highest altitudes, which is described in section 2.

(b) As a cross-track instrument scans toward nadir, its lowest sounding channels become more sensitive to variations in surface emissivity because of the decreasing atmospheric path length. However, the impact of this greater sensitivity on retrieval accuracy depends on how these channels are used in the retrieval algorithm. In an optimum algorithm, the shift of all weighting functions to lower altitudes would cause a compensating lesser weight to be given, at any fixed altitude, to the channel that peaks closest to the surface. This effect can be studied by means of numerical simulations.

(c) In general, the lower-atmosphere channels become more sensitive to clouds and precipitation as θ decreases, because the shielding effect of the atmosphere overlying the clouds decreases. However, retrievals are done as a function of altitude rather than frequency. The peak altitude of a weighting function is approximately at the

Corresponding author address: Philip W. Rosenkranz, Research Laboratory of Electronics, Room 26-343, Massachusetts Institute of Technology, 77 Massachusetts Ave., Cambridge, MA 02139-4307.
E-mail: pwr@mit.edu

point in the atmosphere where the optical depth is unity. Hence, a channel whose weighting function peaks at a given altitude for $\theta \sim 0$ would have to be closer to the center of the absorption band than a channel that peaks at the same altitude for a large θ. Consider two hypothetical channels with the same clear-atmosphere peak altitude, one for a vertical path and the other for a slanting path; they would have nearly the same total gaseous opacity along their different paths, but the opacity of a planar cloud added to the atmosphere would be greater by the factor secant θ, where θ is the incidence angle for the slant path. (Assuming that the two frequencies are close together, the liquid water absorption per unit distance would be nearly the same.) This qualitative reasoning implies that, given an optimum retrieval algorithm, accuracy near nadir would be impacted less severely than at larger angles. However, numerical simulations are necessary for a quantitative comparison, because the impact of clouds can be rather complex, varying with frequency, incidence angle, and surface emissivity.

(d) Cross-track scanning instruments can be calibrated by pointing the beam at cold space and at a target on the instrument. With a conical scan, the main reflector never points in those directions; at best, a subreflector can be moved into position to direct energy from cold space or a target into the instrument feed. Then it is necessary to rely on prelaunch calibration of losses in the main reflector.

(e) Because a cross-track scan measures a range of angles, the retrieval algorithm is necessarily more complicated than for a fixed angle. This consideration does not bear directly on the accuracy of the retrievals, but if the algorithm yields biased results, the biases may be angle-dependent.

(f) Compatibility with other instruments must also be considered. Sounding with infrared wavelengths is possible only in clear air or through broken clouds, and cloud-clearing algorithms decrease in accuracy as the percentage of cloud cover increases. Given some vertical cloud extent, this percentage will tend to increase at oblique angles. Hence, a cross-track scan is preferred for infrared sounders. If microwave channels are to be combined with infrared channels in a retrieval algorithm, greater complexity is involved in registering a conical microwave sounder, because its slanting path through the atmosphere is different from that of the cross-track infrared sounder, and thus the mapping depends on altitude. On the other hand, imaging of surface parameters with microwaves is best done with dual-polarization at oblique incidence (among other reasons, to separate the effects of near-ocean-surface wind speed from other parameters). The problem of registration of conical-scanned microwave window channel measurements with a cross-track sounder would probably be less difficult, because the radiation measured by the former originates close to the surface. However, a cross-track sounder needs at least one window channel to provide
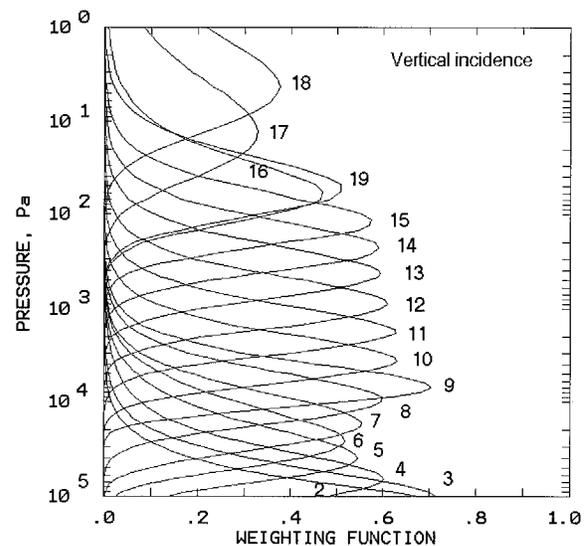

FIG. 1. Weighting functions at vertical incidence in the magnetic field at 45°N, 60°W, with surface emissivity of 0.9.

surface emissivity averaged over exactly the same instantaneous field of view as the sounding channels.

(g) Other relevant questions include engineering feasibility and impact on overall system cost.

In this paper, we examine the impact of points (a), (b), and (c) (for nonprecipitating clouds) on retrieval accuracy using microwave channels alone. For the case of precipitation, a planar model is probably not realistic, and if sounding through precipitation is excluded as a yet-unsolved retrieval problem, the impact of precipitation is on retrieval yield rather than accuracy. Section 6 below considers this effect with a simple rain-cell model. We will not consider here the impact of scan design on retrieval of geophysical parameters other than temperature.

2. Weighting functions

Figures 1 and 2 show temperature weighting functions of the channels under consideration, at $\theta = 0°$ and 70°, respectively, for a magnetic field value of 51 μT (location 45°N, 60°W). Table 1 describes the characteristics of the channels. We consider the sensitivity values to be achievable with the current state of microwave technology. A complete instrument would also have window channels and water vapor channels, which would be used to supply measurements of surface brightness and moisture to the temperature retrieval algorithm. The weighting functions of channels close to the line centers (14–20) depend on the terrestrial magnetic field strength and orientation because of oxygen's magnetic dipole moment, as discussed by Rosenkranz and Staelin (1988) and Stogryn (1989a,b). For example, in the Southern Hemisphere the relative positions of channels 16 and 18 would interchange. At pressures higher than a few hectopascals, pressure broadening
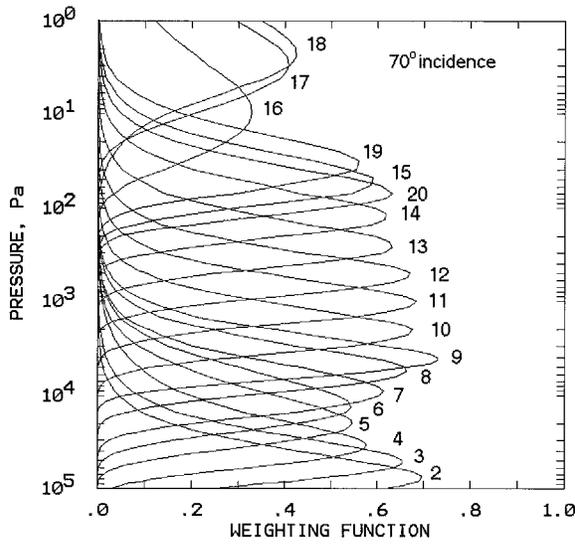
FIG. 2. As in Fig. 1 but at 70° incidence angle. The Doppler shift is set to zero in this figure.

overcomes the magnetic (Zeeman) effect. In the case of conical scanning, an extra channel (20) is included because the observed line frequency will shift during a scan due to the Doppler effect associated with the component of satellite motion along the line of sight.

As shown in Figs. 1 and 2, we have chosen 18 or 19 channels distributed over five decades in pressure. These could be compared with soon-to-be-launched sounding instruments such as the Advanced Microwave Sounding Unit-A (AMSU-A), which has 11 sounding channels covering three decades of pressure, or the Special Sensor Microwave/Imager Sounder (SSM/IS), with 12 temperature sounding channels distributed over five decades in pressure.

The altitude resolution of weighting functions is related to the rate at which absorption increases with depth in the atmosphere. For this reason, weighting functions of channels located close to line centers (e.g., 16–18) are less sharply peaked in altitude than those farther out on the wings. Likewise, the weighting function of a given channel tends to become slightly sharper with increasing incidence angle because it peaks at lower pressure, where the lines are narrower. This latter effect is offset on some channels by other effects such as changing magnetic field direction or temperature lapse rate.

3. Retrieval method

The primary focus of this paper is on the relative performance of two scan modes. Provided that a retrieval algorithm uses the information contained in the measurements in an approximately optimum way [in the sense used in paragraphs (b) and (c) of section 1], the details of the algorithm are of secondary consequence in this context. However, we will describe the algorithm in sufficient detail to fully communicate the meaning of the results presented here. Retrieval of the atmospheric temperature profile from brightness temperature measurements would follow these steps.

(a) The initial-guess profile T_g is formed by a minimum-variance combination of the previous nearby retrieval T^* and an a priori (here, the global mean) profile $\langle T \rangle$:

$$T_g = \rho T^* + (1 - \rho) \langle T \rangle. \quad (1)$$

The parameter ρ represents the horizontal autocorrelation between the previous retrieval and the current location. Various studies (e.g., Briancon and Staelin 1985) have shown that within distances of a few hundred ki-

TABLE 1. Channel specifications. Note that $f_{7+} = 60\,434.78$ and $f_{9+} = 61\,150.56$. Channels 14–20 have right-circular polarization.

Channel no.	Passband center frequencies (MHz)	Passband widths (MHz)	Sensitivity (K)
2	51 760	400	0.22
3	52 800	400	0.22
4	53 596 ± 115	2 × 170	0.23
5	54 400	400	0.21
6	54 940	400	0.21
7	55 500	330	0.22
8	56 020, 56 670	270, 330	0.17
9	60 793	330	0.22
10	$f_{7+} + 105, f_{9+} - 105$	2 × 78	0.33
11	$f_{7+} - 56, +48, f_{9+} \pm 48$	44,3 × 36	0.34
12	$f_{7+} \pm 22, f_{9+} \pm 22$	4 × 16	0.53
13	$f_{7+} \pm 10, f_{9+} \pm 10$	4 × 8	0.75
14	$f_{7+} - 4.5, f_{9+} - 4.5$	2 × 3	1.75
15	$f_{7+} - 2.1, f_{9+} - 2.1$	2 × 0.8	3.36
16	$f_{7+} - 1.0, f_{9+} - 1.0$	2 × 0.5 (0.8)*	4.10 (3.36)*
17	f_{7+}, f_{9+}	2 × 1.0 (0.8)*	2.90 (3.36)*
18	$f_{7+} + 1.0, f_{9+} + 1.0$	2 × 0.5 (0.8)*	4.10 (3.36)*
19	$f_{7+} + 2.1, f_{9+} + 2.1$	2 × 0.8	3.36
20*	$f_{7+} + 3.2, f_{9+} + 3.2$	2 × 0.8	3.36

* For conical scan only.

lometers the horizontal temperature autocorrelation function is quasi-exponential with scale length typically about 1000 km. In this study, ρ was set to the value 0.95 at all levels, for 50-km separation. Equation (1) reduces the mean error that would otherwise result from use of a global-mean initial guess.

(b) A window channel measurement is corrected for atmospheric attenuation and emission to obtain an estimate of the surface brightness temperature for the sounding channels. This correction could involve other window channels and water vapor channels that are not used in the retrieval of temperature. The temperature-sounding channels that are sensitive to the surface are sufficiently close in frequency that we need not consider possible differences of surface brightness among them. Surface skin temperature will be considered part of the temperature profile vector. Thus, the state parameters pertaining to the surface are temperature and brightness temperature, rather than temperature and emissivity.

(c) Weighting functions and brightness temperatures for each of the sounding channels are computed from the initial-guess profile and the estimated surface brightness, using a rapid transmittance model (Rosenkranz 1995) and the International Geomagnetic Reference Field (IGRF) model. Any Doppler shift of the lines is taken into account at this point.

(d) The temperature profile for the current location is retrieved by a minimum-variance method (Rodgers 1976):

$$\mathbf{T}^* = \mathbf{T}_g + \mathbf{D}(\mathbf{T}_B - \mathbf{T}_{Bg}), \qquad (2)$$

where $\mathbf{T}_B$ is a vector containing the measured brightness temperatures, $\mathbf{T}_{Bg}$ is the vector of computed brightness temperatures, and

$$\mathbf{D} = \mathbf{S}_g \mathbf{W}_g^{\mathrm{T}} (\mathbf{W}_g \mathbf{S}_g \mathbf{W}_g^{\mathrm{T}} + \mathbf{N})^{-1}, \qquad (3)$$

where $\mathbf{S}_g$ is the assumed covariance matrix of the vector $\mathbf{T}_g$, $\mathbf{W}_g$ is a matrix whose rows correspond to the weighting functions (superscript T denotes the transpose), and $\mathbf{N}$ is the covariance matrix of measurement errors.

4. Error analysis

An iterated calculation was used to simulate the errors that would result from the recursive procedure described in section 3. It was assumed that the retrieval process would start with an assumed global mean temperature profile and covariance matrix corresponding to a set of 715 profiles assembled by NOAA (D. Wark 1986, personal communication). It is necessary to consider that the assumed covariance matrix $\mathbf{S}_g$ may differ from the true covariance $\mathbf{S}_t$; also, the weighting matrix $\mathbf{W}_g$ differs from the actual weights $\mathbf{W}_t$, first because $\mathbf{W}_g$ depends on $\mathbf{T}_g$ which is not equal to the true $\mathbf{T}$, and second because of transmittance modeling errors. The "true" mean profile and covariance were obtained from either of two sources: the TIGR ensemble (Chedin et al. 1985; Escobar 1993) of 1761 profiles, which is subdivided into

five airmass types; or a set of 84 selected rocket-launched passive sphere soundings, whose maximum altitudes all exceeded 80 km. The TIGR profiles were used to test sounding performance at pressures greater than 5 hPa, the rocket profiles at 5 hPa or less. In order to account for surface–air temperature differences when the covariance matrices were computed, the surface skin temperature was assigned a variance $(4 \text{ K})^2$ higher than the near-surface air temperature, and the same covariances with other levels.

Surface brightness temperature was included as one element of the temperature vector, with a prior (i.e., as estimated from the window channel) rms uncertainty of $4 \sec\theta$ in kelvins. This uncertainty estimate is based on experience with the SSM/I instrument (Rosenkranz 1992).

The mean profile error is

$$\mathbf{E}_{\mathrm{mean}} = \mathbf{D}(\langle \mathbf{T}_B \rangle_t - \langle \mathbf{T}_{Bg} \rangle) + \langle \mathbf{T}_g \rangle - \langle \mathbf{T} \rangle_t, \qquad (4)$$

where angle brackets indicate an average over the statistical ensemble of initial-guess profiles and angle brackets with subscript t indicate an average over the ensemble of true profiles. Note that $\mathbf{E}_{\mathrm{mean}}$ is not averaged over different magnetic fields. The covariance matrix of profile errors is given by

$$\mathbf{S}_E = (\mathbf{I} - \mathbf{D}\mathbf{W}_t)\mathbf{S}_t(\mathbf{I} - \mathbf{D}\mathbf{W}_t)^{\mathrm{T}} + \mathbf{D}\mathbf{N}\mathbf{D}^{\mathrm{T}}. \qquad (5)$$

The first term on the right side above is called the null-space error by Rodgers (1990) and the second term is the projection of measurement errors onto the space of temperature profiles. The sum of the diagonal element of $\mathbf{S}_E$ plus $\mathbf{E}_{\mathrm{mean}}^2$ is the total mean-square error at each level.

On the first iteration, $\mathbf{T}_g$ was the assumed global mean profile and $\mathbf{S}_t$ was set equal to $\mathbf{S}$, the a priori covariance about the mean of the true ensemble of profiles. On the second iteration, the initial guess was calculated from (1), and its true covariance from

$$\mathbf{S}_t = \rho^2 \mathbf{S}_E + (1 - \rho^2)\mathbf{S}, \qquad (6)$$

where $\mathbf{S}_E$ on the right side is the result of the first iteration. The assumed covariance $\mathbf{S}_g$ was not changed on the second iteration, for economy of computation. Equation (6) simulates the prior uncertainty of the profile at the second location after starting the retrieval process. It was found that the second iteration of (5) gave a good approximation to the asymptote of the process. The only purpose of iteration here is to simulate the recursion implied in Eq. (1); radiative transfer nonlinearities are very small.

The mean and null-space errors calculated as above and plotted in the next section include the effect of approximations made in the rapid transmittance algorithm, but not of possible errors in the line-by-line calculation on which it is based. The sources of error in the latter are (a) uncertainties in the measurements of line parameters; the effect of these on upward-propagating brightness temperatures is expected to be small,
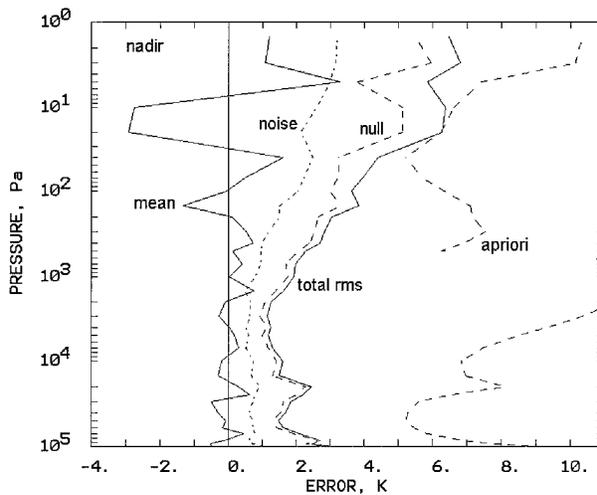
FIG. 3. Total rms temperature retrieval error and its components, using the weighting functions of Fig. 1.

FIG. 4. Total rms temperature retrieval error and its components, using the weighting functions of Fig. 2.

and mainly a bias error; (b) variations in the mixing ratio of molecular oxygen; these are considered negligible at the altitudes of interest; and (c) deviation of the terrestrial magnetic field from the IGRF model. For quiet field conditions these errors should be on the order of 0.3 μT or less, but very severe magnetic storms can cause disturbances of 1 μT, which could perturb the most sensitive channels (16 and 18) by as much as 2 K, an error comparable to their sensitivity.

5. Results

Error profiles have been computed for various incidence angles, magnetic field configurations, and values of Doppler shift. However, only a few typical results are shown here. Figure 3 plots the mean, noise, and null-space errors and also the total rms error for a clear-air sounding at nadir. Figure 4 shows these errors at $\theta = 70°$. The highest levels have large bias errors that are the result of unresolved vertical structure, possibly gravity waves, in some of the 84 rocket soundings. This structure may also be in part an artifact of the transition from supersonic to subsonic sphere fall rate (see von Zahn and Meyer 1989). The a priori curve shows the standard deviation of the test ensemble; the discontinuity at 5 hPa is due to use of different profile test ensembles above and below this level.

Comparison of Figs. 3 and 4 shows that the null-space and noise components are both slightly smaller in Fig. 4 in the stratosphere. These differences result from the previously noted change in sharpness of weighting functions with θ and from the fact that the channels that peak at given heights are farther out on line wings in Fig. 4 and therefore have larger passband widths and better sensitivity.

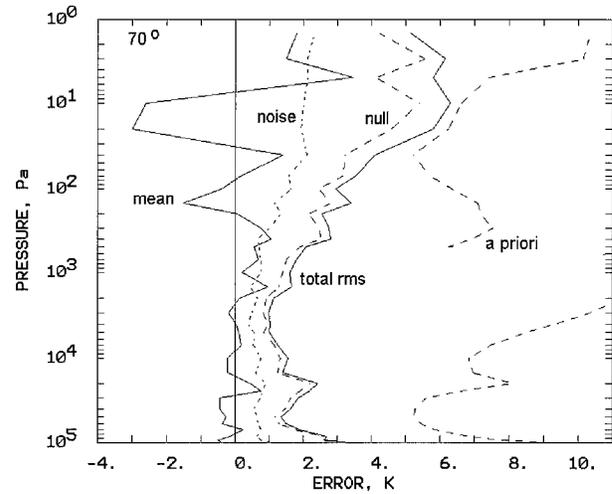The largest error component in Figs. 3 and 4 is the null-space error. However, this presentation may be overly pessimistic because it includes any deviation from the ideal of an exact reproduction of the true profile of temperature at each level. A retrieval of this type produces a smoothed version of the true profile, and for some purposes, such as the detection of atmospheric planetary waves (e.g., Austen et al. 1976), this vertical smoothness is not an obstacle.

Figure 5 compares total rms errors in midlatitudes for a 70° conical scan with the weighted average for a cross-track scan. These errors include the perturbations caused by two cloud models: low (850–1000 hPa) and middle (500–600 hPa), both having 150 g m^{-2} liquid water content, and occurring with probabilities that depend on time of day and type of surface, as determined from ISCCP statistics by Carlson and Wolf (1993); see Table 2. High clouds are assumed to be frozen and would therefore have little microwave absorption. The low and middle cloud models have opacities of approximately 0.05 sec θ at the frequencies used here. As long as its opacity is less than unity, the perturbation introduced by a cloud model at a given altitude is roughly proportional to its opacity, hence to its liquid water content. Our cloud weight is somewhat greater than the rms of nonprecipitating cloud liquid-water distributions found by Liu and Curry (1993). In their statistics, approximately 90% of nonprecipitating cloud pixels (at 30-km resolution) had liquid water less than 150 g m^{-2}. In the lower troposphere, slightly better performance is obtained from the cross-track scan because of less sensitivity to clouds, on average, with smaller incidence angles. In the mesosphere, slightly better performance is obtained from the conical mode because the weighting functions are higher on average than with a cross-track scan.

6. Precipitation model

Rain clouds contain much more liquid water than nonprecipitating clouds and to a first approximation,
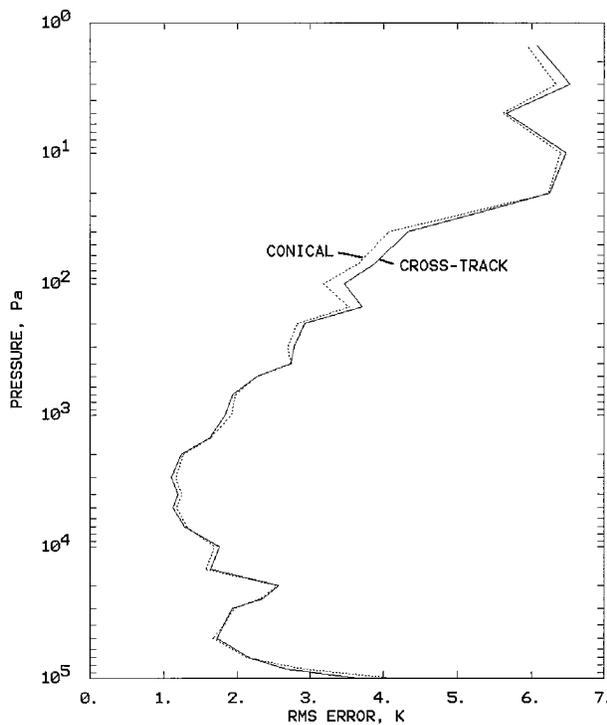
FIG. 5. The rms error profiles for a 70° conical and a cross-track scan in midlatitudes, averaged over land–ocean surfaces and occurrence probabilities of nonprecipitating clouds. The cross-track profile is also averaged over the number of pixels at each incidence angle.

they can be considered opaque in the greater than 50-GHz frequency range of interest here. Scattering from ice, if present, above the freezing level exacerbates the effect on brightness temperatures. At a spatial resolution of about 50 km, however, the radiometer beam typically is not completely filled by rain. During the GARP (Global Atmospheric Research Program) Atlantic Tropical Experiment, for example, beamfilling for a 25-km field of view averaged 60%, given the presence of rain (Short and North 1990). Although the probability of observing precipitation should not vary appreciably with θ (given a specified spatial resolution), the beamfilling factor can increase with θ, depending on the geometry of the rain clouds. Accurate temperature sounding in the presence of significant amounts of precipitation has not yet been successfully demonstrated, and if such situations are rejected, there will be a dependence of retrieval yield on θ.

A rough estimate of the angle dependence of beamfilling can be obtained with a simple model. We assumed cylindrical rain cells with a height of 4 km and diameter of 10 km, randomly distributed over a 400 km × 400 km area. The height corresponds to a subtropical freezing altitude, and the diameter represents a medium-sized rain cell, as inferred from the data of Gasiewski and Staelin (1989). The cells were allowed to overlap, thus occasionally forming some larger structures. The shape of the probability distribution for the beamfilling factor

TABLE 2. Diurnal cycle of the annual average cloud amounts (percent) at low and middle levels, in the region 60°S–60°N (from Carlson and Wolf 1993).

	Local time of day (hours)			
	0000	0600	1200	1800
Low cloud over land	5	5.5	20	10
Low cloud over ocean	35	35	33.5	32
Middle cloud over land	18	18.5	16	16.5
Middle cloud over ocean	17	17.2	14.8	15.8

depends on spatial resolution, but this large area was used in order to obtain a meaningful average value.

Figure 6 plots the average area-filling factor, defined as the projected cell area divided by total area, as a function of incidence angle θ for two values of the number of cells. As seen by comparison with the dotted line, angular variation of filling for the rain-cell model is less steep than the $\sec\theta$ variation of path length in an optically thin planar cloud model. Still, the filling factor increases by a factor of 1.4–1.7 in going from nadir to 70°. A conical scan at 70° has beamfilling greater by a factor 1.2–1.4 than the weighted-average value for a cross-track scan, plotted in Fig. 6 as crosses at the 70° maximum angle.

It is known that the fraction of a large area for which the rainfall rate exceeds a given threshold is highly correlated with the instantaneous area-averaged rainfall rate (Atlas et al. 1990). If we choose an appropriate threshold, we can identify this fractional area with the beamfilling factor for a vertical field of view. Hence, for an oblique field of view, a sounding (at a fixed altitude) would be perturbed equally by a lower average rain rate than for the vertical view, corresponding to the inverse of the geometric beamfilling factor. In other words, the number of rain situations causing unacceptable sound-
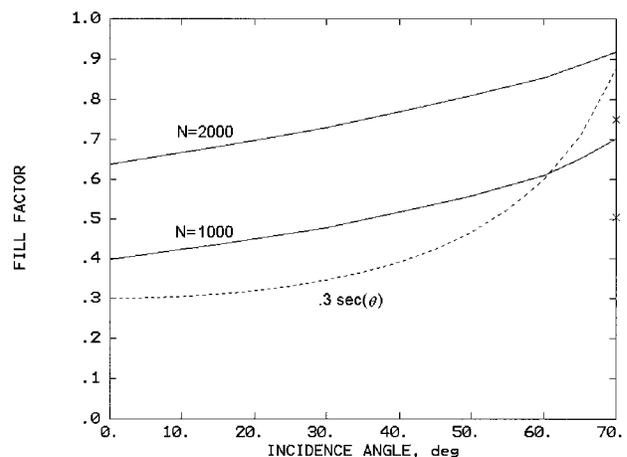

FIG. 6. Area-filling factor for a cylindrical rain-cell model for two values of the number of cells in a 400 km × 400 km area. The crosses are filling factors averaged over the number of pixels at each incidence angle for a cross-track scan. The dotted line shows a function proportional to $\sec\theta$.

ings would increase with incidence angle. The actual number of such soundings will depend also on spatial resolution, on the probability distribution of rain rates, and perhaps on the retrieval algorithm. High-resolution microwave sensors, such as those that will be carried by the NOAA-K satellite and the Tropical Rainfall Measuring Mission, should provide a database for more elaborate modeling of precipitation effects.

7. Summary and conclusions

A choice of scan mode for a microwave sounder involves the trade-off of numerous factors including engineering and calibration issues, retrieval algorithm performance, and compatibility with other sensors. We have addressed a few of these many questions in relation to temperature profiling and found some small but noticeable differences in overall-average rms sounding accuracy outside of precipitating regions. These differences favor the conical design for some altitudes and the cross-track design for others. We did not attempt to simulate radiative transfer in precipitation, but a consideration of the geometry of the problem leads to the conclusion that, due to this factor, retrieval yield would be lower with the conical design.

The retrieval accuracies discussed here used only microwave channels. If an infrared sounder is present on the satellite, the accuracy of the complete sounding system, combining microwave and infrared, would be the measure of performance. This consideration may make compatibility of scan mode between infrared and microwave channels the decisive factor, given the small differences found here in microwave-only retrievals.

REFERENCES

Atlas, D., D. Rosenfeld, and D. A. Short, 1990: The estimation of convective rainfall by area integrals. 1: The theoretical and empirical basis. *J. Geophys. Res.,* **95,** 2153–2160.

Austen, M. D., and Coauthors, 1976: Satellite observations of planetary waves in the mesosphere. *Nature,* **260,** 594–596.

Briancon, A., and D. H. Staelin, 1985: Modeling the three-dimensional macrostructure of atmospheric temperature fields for the purpose of remote sensing. *1985 Int. Geoscience and Remote Sensing Symp. Digest,* Amherst, MA, Institute of Electrical and Electronics Engineers, 357–362.

Carlson, B., and A. B. Wolf, 1993: Spatial and temporal characterization of diurnal cloud variability. Preprints, *Fourth Symp. on Global Change Studies,* Anaheim, CA, Amer. Meteor. Soc., 98–103.

Chedin, A., N. A. Scott, C. Wahiche, and P. Moulinier, 1985: The improved initialization inversion method: A high resolution physical method for temperature retrievals from satellites of the TIROS-N series. *J. Climate Appl. Meteor.,* **24,** 128–143.

Escobar, J., 1993: Base de données pour la restitution de paramètres atmosphériques à l'échelle globale—Etude sur l'inversion par réseaux de neurones des données des sondeurs verticaux atmosphériques satellitaires présents et à venir. Ph.D. thesis, Ecole Polytechnique. [Available from Laboratoire de Météorologie Dynamique, Ecole Polytechnique, 91128 Palaiseau Cedex, France.]

Gasiewski, A. J., and D. H. Staelin, 1989: Statistical precipitation cell parameter estimation using passive 118-GHz O_2 observations. *J. Geophys. Res.,* **94,** 18 367–18 378.

Liu, G., and J. A. Curry, 1993: Determination of characteristic features of cloud liquid water from satellite microwave measurements. *J. Geophys. Res.,* **98,** 5069–5092.

Rodgers, C. D., 1976: Retrieval of atmospheric temperature and composition from remote measurements of thermal radiation. *Rev. Geophys. Space Phys.,* **14,** 609–624.

——, 1990: Characterization and error analysis of profiles retrieved from remote sounding measurements. *J. Geophys. Res.,* **95,** 5587–5595.

Rosenkranz, P. W., 1992: Rough-sea microwave emissivities measured with the SSM/I. *IEEE Trans. Geosci. Remote Sens.,* **30,** 1081–1085.

——, 1995: A rapid transmittance algorithm for microwave sounding channels. *IEEE Trans. Geosci. Remote Sens.,* **33,** 1135–1140.

——, and D. H. Staelin, 1988: Polarized thermal microwave emission from oxygen in the mesosphere. *Radio Sci.,* **23,** 721–729.

Short, D. A., and G. R. North, 1990: The beam filling error in the Nimbus 5 electronically scanning microwave radiometer observations of Global Atlantic Tropical Experiment rainfall. *J. Geophys. Res.,* **95,** 2187–2193.

Stogryn, A., 1989a: The magnetic field dependence of brightness temperatures at frequencies near the O_2 microwave absorption lines. *IEEE Trans. Geosci. Remote Sens.,* **27,** 279–289.

——, 1989b: Mesospheric temperature sounding with microwave radiometers. *IEEE Trans. Geosci. Remote Sens.,* **27,** 332–338.

von Zahn, U., and W. Meyer, 1989: Mesopause temperatures in polar summer. *J. Geophys. Res.,* **94,** 14 647–14 651.

Waters, J. W., 1993: Microwave limb sounding. *Atmospheric Remote Sensing by Microwave Radiometry,* M. A. Janssen, Ed., Wiley, 383–434.